Supporting Information

Mohan et al. 10.1073/pnas.1413731111

SI Text

SI Methods

Small Subunit Structures. We have included small subunit structures of 55 ribosome complexes from the Protein Data Bank (PDB) (1) as listed in Table S1. The structures include ribosome complexes trapped in different states and under different experimental conditions and include various bound ligands and antibiotics. Of the 55 complexes, 10 entries are cryo-EM–derived bacterial ribosome complexes. Forty-one complexes are 70S bacterial ribosome crystal structures, reported at a resolution of at 4 Å or better. We included three eukaryotic complexes to compare with the results obtained from bacterial ones, to identify possible similarities in their mechanics of head rotation.

Assigning the Core Body Domain of 16S rRNA. We first defined the core 16S body positions that remain static during head rotation. By structural superimpositions of 16S rRNAs on the body domain (between nucleotide positions 1–920 and 1397–1542) in PyMOL (2), the core body domain was assigned as positions that remain within 0.8-Å rmsd between all 41 bacterial 16S rRNAs. All further 30S subunit superimpositions were defined on the core body domain.

The Euler–Rodrigues Formula for Domain Motions. Euler's rotation theorem states that any movement between connected domains can be expressed as a single rotation around an axis. For a rigid-body rotational event, applying the Euler–Rodrigues (E–R) formula (below) will generate an axis and a corresponding angle of rotation. In this analysis, the 10 cryo-EM–derived structures are included because atomic-level detail is not required. To apply the E–R formula to 30S head movement in each structure and to visualize the E–R axis for head rotation, we created a plug-in module for PyMOL (2). The plug-in can be downloaded from http://rna.ucsc.edu/rnacenter/erodaxis.py.

The mobile structure was first aligned to the reference structure in PyMOL. PyMOL generates a composite 4 × 4 transformation matrix containing a 3 × 3 rotation (R) matrix and 3 × 1 translation (T) matrix, for this alignment. The angle (Θ) of rotation is derived from the E–R formula on the diagonal elements of the rotation matrix as

$$\Theta = \cos^{-1}\left(\frac{R_{00}+R_{11}+R_{22}-1}{2}\right).$$

The direction of the axis is calculated as

$$V_x = \frac{R_{21}-R_{12}}{2\sin\Theta}$$

$$V_y = \frac{R_{02}-R_{20}}{2\sin\Theta}$$

$$V_z = \frac{R_{10}-R_{01}}{2\sin\Theta}.$$

The origin of the axis can be defined as $O = \mathrm{inv}(R-I)T$, where I is a 3 × 3 identity matrix. Thus, the directional vector $\vec{v}$ defines the axis of rotation passing through the point O.

We determined that the 16S rRNA coordinates from Selmer et al. (3) (PDB ID code 2J00) display the lowest degree of head rotation, which we defined as 0°, and is our reference unrotatedstructure. Positive head rotation is defined as counterclockwise movement of the head domain in a given ribosome with respect to the reference structure. For eukaryotic structures, Rabl et al. (4) (PDB ID code 2XZN) was assigned as the reference structure.

Body Rotation. To identify possible correlations between 30S head rotation and intersubunit (i.e., body) rotation, we applied the E–R formula separately to the head and body domains for each structure, retaining 2J00 as the reference structure for consistency. Positive body rotation is also defined as counterclockwise, as viewed from the solvent face of the 30S subunit.

Defining Core Helices. We identified the molecular boundary between the static (body) and mobile (head) domains associated with the 30S head rotation, and defined a series of near-coaxial helices (h28–h29–h30–h32–h34–h35–h36) which traverse through the 16S rRNA head domain (5) to define the core of the 16S rRNA component of the 30S head domain. All crystal structures (including eukaryotic structures) in our dataset showed remarkable conservation in the lengths of their core helices.

Helical Axis. We restricted this analysis to the subset of 41 bacterial crystal structures in our dataset. We applied Curves+ (6) to define the helical axis in each 16S rRNA (called the CUR axis here), based on the atomic positions of the base pairs.

Identification of Inflection Points. To identify the point of inflection and nature of hinging across the crystal structures, the coordinates of the CUR axis were grouped according to head and body rotation classes (Table 1). The average magnitude of deviation of the CUR axes (ΔCUR) at each position for each group, with respect to the corresponding average CUR positions in classical-state complexes was calculated using Matlab (7). A plot of ΔCUR vs. axis position was made to identify the origins of movement of the head domain.

Correlating Changes in Nucleotide Positions with 30S Head Rotation. To understand the molecular changes at each hinge, we analyzed the nucleotide positions within the hinge regions for each of the 41 crystal structures (hinge 1 positions: 920–933 and 1384–1396; hinge 2 positions: 1060–1083, 1102–1107, and 1188–1197). Because the resolution of the structures in our dataset is not uniform, we focused our analysis on phosphorus backbone atoms whose positions can be most accurately determined. In each 16S rRNA, we calculated distances, angles, and dihedral angles for consecutive backbone phosphorus atoms and the results for each position across 41 structures were plotted as a function of increasing head rotation, using Matlab. The correlation coefficient for each measurement, with respect to increasing head rotation, was also calculated using Matlab.

Analysis of Variation at Each Hinge. To identify the magnitude of change at each hinge during head rotation, we applied the E–R formula to the helical axes flanking each hinge for each of the 41 crystal structures, with respect to the reference state. The angular change at each hinge was plotted with respect to head rotation, and with respect to each other, using Matlab. Correlation coefficients for the angular change were also calculated using Matlab.

SI Discussion

30S Head and Body Rotation Classes. Our dataset comprises 52 bacterial ribosome structures (41 crystal structures at 4 Å or better and 1 at 5.5 Å; and 10 cryo-EM–derived structures) and three eukaryotic ribosome structures (Table S1). The observed

range of head rotation is near-continuous from 0 to 21.3° (Table 1 and Table S1); however, head rotation values for complexes containing full-length tRNAs are constrained more narrowly into three distinct ranges which correspond with the binding states of the tRNAs in the respective complexes. These three ranges are (I) low (0–4°), for classical A/A, P/P or E/E states; (II) intermediate (5–7°), hybrid A/P or P/E states; and (III) high (18–21°), chimeric hybrid ap/P or pe/E states, inclusive of X-ray and cryo-EM–derived data. We refer to these three classes as (I) classical (Cla), (II) hybrid (Hyb), and (III) chimeric hybrid (Chi). Our dataset was restricted to the 41 bacterial ribosome crystal structures when identifying hinge regions, where the average head rotations are Cla, 2.0 ± 1.0°; Hyb, 5.9 ± 0.7°; and Chi, 19.2 ± 1.3° (Table 1). In contrast, head rotation values vary over a 10° range (6.9–16.4°) among ribosomes with vacant tRNA-binding sites (Table S1) and do not appear to correlate with the presence of bound factors or other ligands. Head rotation was again measured relative to the classical-state structure (3) (2J00), with the lowest head rotation.

We also calculated the values for 30S body rotation (i.e., overall rotation of the 30S subunit relative to the 50S subunit) in these same complexes, using the E–R formula, to identify possible correlations with head rotation. Body rotation was again measured relative to the classical-state structure, with positive rotation defined as counterclockwise, as viewed from the solvent face of the 30S subunit (Fig. S1*A*). Values for 30S body rotation varied over a 13° range between −3.5° and 9.7° across the dataset (Table 1 and Table S1). In general, head and body rotations appear to be uncoupled (Fig. S1*B*). However, as observed for head rotation, complexes bound with full-length tRNAs in similar binding states have similar body rotations (Cla −0.4 ± 0.1°; Hyb, 6.7 ± 2.0°; Chi, 2.1 ± 1.0°) (Table 1).

Although complexes with vacant tRNA-binding sites span a variable range of head rotations, the 21 vacant bacterial crystal structures fall into three recognizable subclasses showing similar magnitudes of head rotation and body rotation, all of whose characteristic rotational values are distinct from those of the tRNA-containing structures (Table 1). We term these subclasses vacant 1 (head rotation: 8.1 ± 0.1°; body rotation: −3.3 ± 0.1°), Vacant 2 (head rotation: 11.5 ± 1.3°; body rotation: 4.9 ± 1.9°) and vacant 3 (head rotation: 16.3 ± 0.1°; body rotation: −2.4 ± 0.1°) (Table 1). Interestingly, even though complexes containing tRNA anticodon stem-loop fragments (ASLs) have a relatively low magnitude of head rotation, the combination of their head and body rotations distinguishes them from the classical-state structures (head rotation: 3.2 ± 1.3°; bod rotation: 2.0 ± 3.8°) (Table S1).

Additionally, we found 65 crystal structures of 30S subunits in the PDB. Values for head rotation fall between 3° and 7°, within the range observed for head rotation in 70S ribosomes.

E–R Axis Orientations. Within each rotation class (Table 1), complexes bound with one or more full-length tRNAs have closely overlapping E–R axes (Fig. S2). Conversely, for similar degrees of head rotation, complexes with vacant tRNA-binding sites show much more divergent orientations of their E–R axes (Fig. S2). This indicates that the presence of bound full-length tRNAs influences and restricts the orientation of the 30S head domain by limiting its degrees of freedom.

Sugar Puckering at Hinge 1. The universally conserved A1503 in the 30S body domain, which has been proposed to act as a translocational pawl (8), remains in contact with hinge 1 at G925 and G927 in the majority of structures with less than 18° of head rotation (Fig. S5*A*). However, in the class III chimeric hybrid (Chi) group, A1503 loses its contact with hinge 1 and instead intercalates between bases -1 and -2 of the mRNA (Fig. S5*B*). This apparent interplay between A1503, hinge 1, and the mRNA suggests a possible mechanism by which head rotation may trigger intercalation of A1503 to prevent back slippage of the mRNA during reverse rotation of the 30S head.

A difference in ribose sugar puckering is accompanied by changes in the backbone torsion angles (9–11), which we calculated using Curves+ (6) and by measuring the dihedral angle between P927 and P928 (defined by P926, P927, P928, and P929). The observed dihedral angle around 927–928 is between −120° and −170° in 36 of the 41 30S ribosome structures, with an average of −140°, corresponding to a 3′-*endo* ribose pucker. However, in the subset of five structures this angle drastically switches, indicating a switch in the pseudorotation angles. These include the four Chi group members, with an average angle of −50°, and one Hyb structure (PDB ID code 3ZVO) (12), with a dihedral angle −12°. The results of backbone dihedral angles calculated using Curves+ yielded similar results.

To control against the possibility that this change in the backbone rotameric state at hinge 1 is an artifact of the crystallographic refinement process in the chimeric hybrid structures, a vacant complex, PDB ID code 1VS7 (13) (16.4° of head rotation, Vac2 group) chosen at random, was refined against the electron density data for the Chi ribosome (PDB ID code 4KBT). The results were consistent with that of 4KBT, i.e., the distance between P927 and P928 in 1VS7 increased to 7 Å from 6 Å. This suggests that ribose 927 at hinge 1 switches from C3′-*endo* to C2′-*endo* sugar puckering with large degrees of 30S head rotation, possibly influenced by the presence of chimeric pe/E or hybrid-state P/E tRNAs.

Twist Parameter. Our results indicate that the primary movement in the neck or h28 is not due to a change in twist for this G-C–rich helix. The correlation of the helical twist parameter, which defines the angle of orientation of successive base pairs, calculated using Curves+, remains at a correlation coefficient of less than 0.5 at each of the 12-bp steps in h28, with varying degrees of head rotation.

1. Bernstein FC, et al. (1977) The Protein Data Bank: A computer-based archival file for macromolecular structures. *J Mol Biol* 112(3):535–542.
2. DeLano WL. The PyMOL Molecular Graphics System (DeLano Scientific LLC, San Carlos, CA).
3. Selmer M, et al. (2006) Structure of the 70S ribosome complexed with mRNA and tRNA. *Science* 313(5795):1935–1942.
4. Rabl J, Leibundgut M, Ataide SF, Haag A, Ban N (2011) Crystal structure of the eukaryotic 40S ribosomal subunit in complex with initiation factor 1. *Science* 331(6018):730–736.
5. Noller HF (2005) RNA structure: Reading the ribosome. *Science* 309(5740):1508–1514.
6. Lavery R, Moakher M, Maddocks JH, Petkeviciute D, Zakrzewska K (2009) Conformational analysis of nucleic acids revisited: Curves+. *Nucleic Acids Res* 37(17):5917–5929.
7. Matlab (2011) Version 7.13: R2011b (The Mathworks Inc.).
8. Zhou J, Lancaster L, Donohue JP, Noller HF (2013) Crystal structures of EF-G-ribosome complexes trapped in intermediate states of translocation. *Science* 340(6140):1236086.
9. Richardson JS, et al.; RNA Ontology Consortium (2008) RNA backbone: Consensus all-angle conformers and modular string nomenclature (an RNA Ontology Consortium contribution). *RNA* 14(3):465–481.
10. Altona C, Sundaralingam M (1972) Conformational analysis of the sugar ring in nucleosides and nucleotides. A new description using the concept of pseudorotation. *J Am Chem Soc* 94(23):8205–8212.
11. Murray LJ, Arendall WB, 3rd, Richardson DC, Richardson JS (2003) RNA backbone is rotameric. *Proc Natl Acad Sci USA* 100(24):13904–13909.
12. Jin H, Kelley AC, Ramakrishnan V (2011) Crystal structure of the hybrid state of ribosome in complex with the guanosine triphosphatase release factor 3. *Proc Natl Acad Sci USA* 108(38):15798–15803.
13. Schuwirth BS, et al. (2006) Structural analysis of kasugamycin inhibition of translation. *Nat Struct Mol Biol* 13(10):879–886.

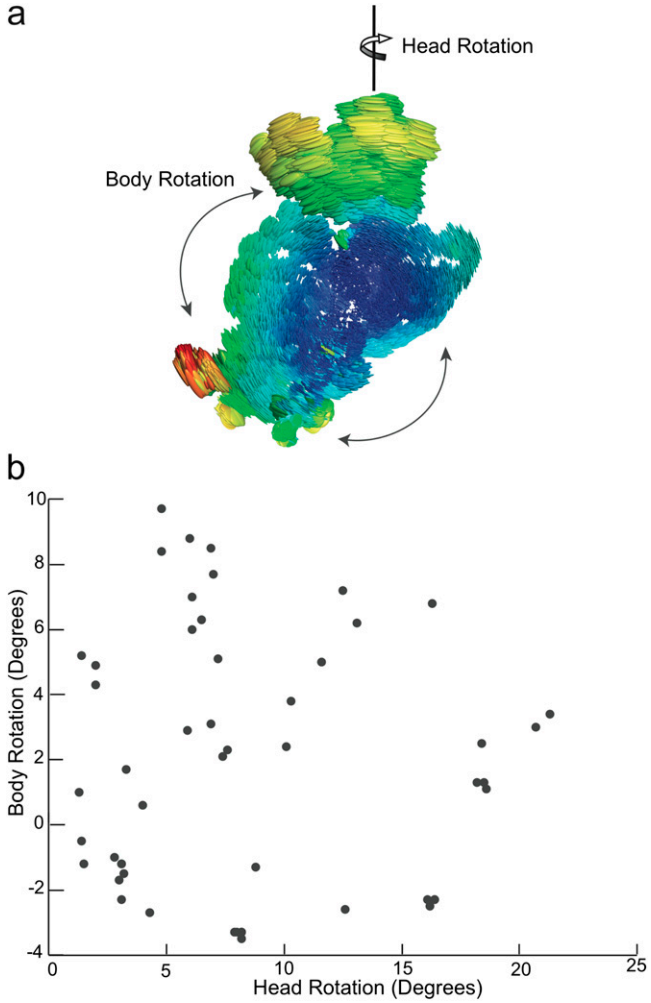

Fig. S1. Head and body rotations across the dataset. (*A*) Using tensor analysis (1), deviations in nucleotide positions in the 16S rRNA are depicted as ellipsoids. rms values are colored as a gradient from least-displaced atoms (purple) to most-displaced atoms (red). Body rotation is defined as the intersubunit rotation of the 30S with respect to the 50S subunit. Here, positive body rotation is defined as counterclockwise, when viewed from the solvent face of the 30S subunit. (*B*) The magnitudes of head and body rotations across 53 structures were calculated using the E–R formula. This graph shows that 30S head and body rotation are not correlated. For similar magnitudes of head rotation, multiple magnitudes of body rotation are possible, and vice versa.

1. Korostelev A, Laurberg M, Noller HF (2009) Multistart simulated annealing refinement of the crystal structure of the 70S ribosome. *Proc Natl Acad Sci USA* 106(43):18195–18200.

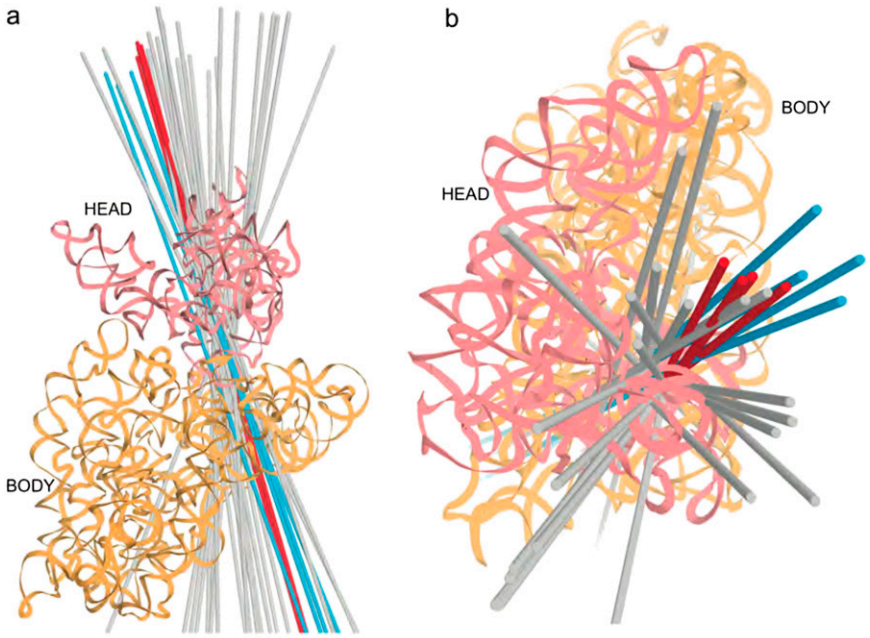

Fig. S2. E–R axis for head rotation. (*A*) Subunit interface and (*B*) top views of the reference state 16S rRNA showing the positions of the E–R axes for crystal structures with head rotation >5°. E–R axes are colored according to the binding state of the tRNA in the complex. P/E hybrid (Hyb) state is in blue, the chimeric (Chi) pe/E state is in red, and the vacant (Vac) ribosomes are in gray. The 16S body domain is shown in orange and the 16S head domain is in pink. E–R axes for the Hyb and Chi structures are relatively restricted in their orientations, indicating that the orientation of the E–R axis is influenced by the presence of tRNA.

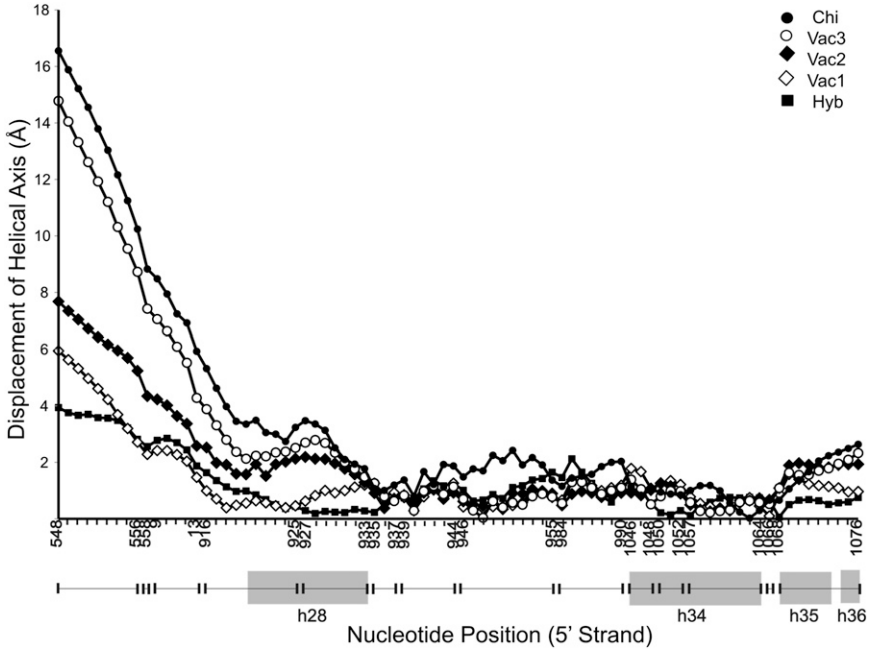

Fig. S3. The head domain moves as a rigid body. The average displacement of helical axes for the core helices in the 30S head domain, for each rotational group (Table 1), is plotted with respect to the classical group for positions along the core axis. The average deviation remains within 2 Å for all structure classes, indicating that the head domain moves as a rigid body.

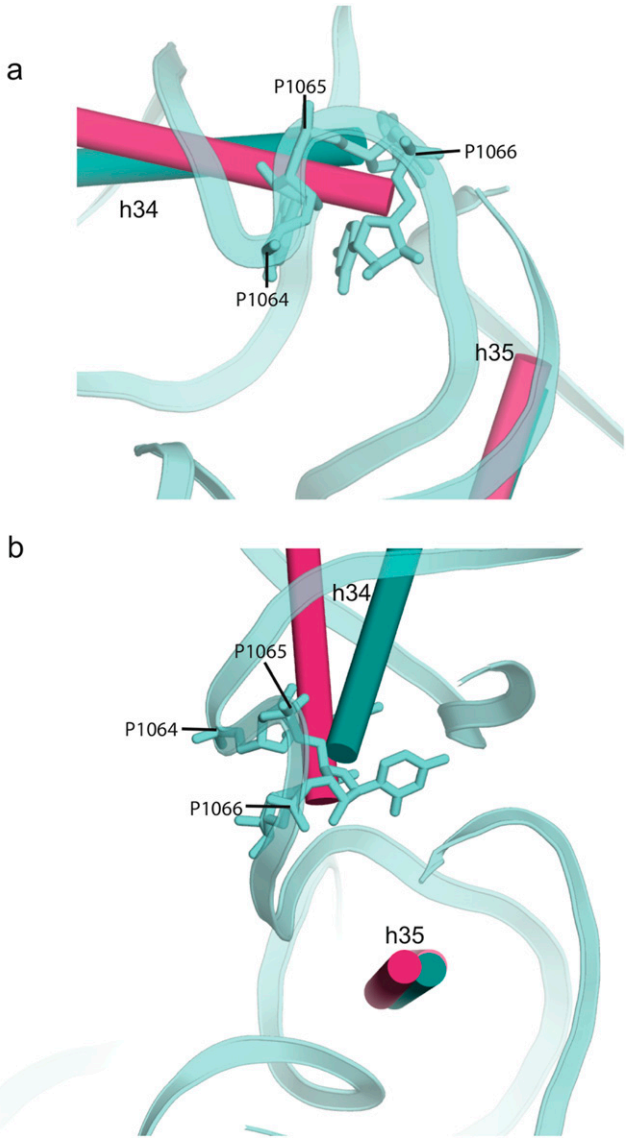

Fig. S4. Close-up view of hinge 2. The angle subtended by P1064–P1065–P1066 decreases by 22° as a result of head rotation. Shown here are the positions of P1064–P1065–P1066. Classical-state 16S rRNA is shown in blue (1). Idealized helical axes at hinge 2 for classical (teal) and rotated (magenta) (2) states are shown, indicating the correlation of flexing at hinge 2 and a change in the position of h34 (and the head domain). For clarity, 16S rRNA of the rotated state has been omitted. See Fig. 4 for details.

1. Selmer M, et al. (2006) Structure of the 70S ribosome complexed with mRNA and tRNA. *Science* 313(5795):1935–1942.
2. Zhou J, Lancaster L, Donohue JP, Noller HF (2013) Crystal structures of EF-G-ribosome complexes trapped in intermediate states of translocation. *Science* 340(6140):1236086.

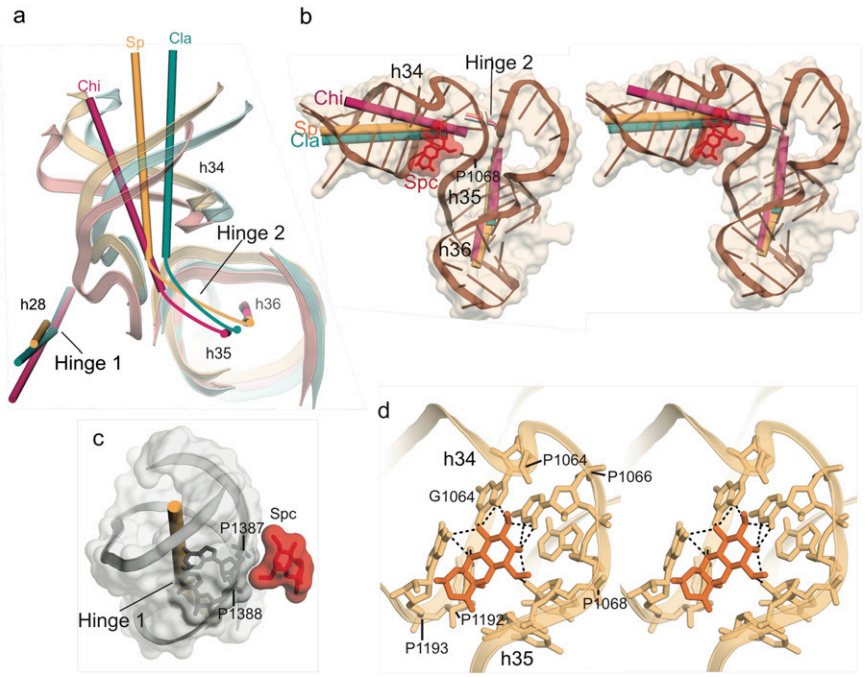

Fig. S5. Spectinomycin-binding site. (*A*) Shown are the positions of h34 in the Cla (1) (cyan), Chi (2) (red), and spectinomycin (Spc) complex (Sp) (3) (orange). In the Spc-containing complex, h34 does not completely swivel toward h28, trapping hinge 2 in an intermediate state of 30S head rotation. (*B*) Stereoview of the spectinomycin-binding site in hinge 2. (*C*) Spc nestles in h28 between the backbone atoms at 1387 and 1388, around the point of contact between hinges, but does not contact the inflection point of hinge 1. (*D*) Stereoview of the contacts formed between Spc (orange) and 16S rRNA (yellow) at Hinge 2, as seen in the ribosome–Spc complexes 2QOU (3) and 1FJG (4).

1. Selmer M, et al. (2006) Structure of the 70S ribosome complexed with mRNA and tRNA. *Science* 313(5795):1935–1942.
2. Zhou J, Lancaster L, Donohue JP, Noller HF (2013) Crystal structures of EF-G-ribosome complexes trapped in intermediate states of translocation. *Science* 340(6140):1236086.
3. Borovinskaya MA, Shoji S, Holton JM, Fredrick K, Cate JHD (2007) A steric block in translation caused by the antibiotic spectinomycin. *ACS Chem Biol* 2(8):545–552.
4. Carter AP, et al. (2000) Functional insights from the structure of the 30S ribosomal subunit and its interactions with antibiotics. *Nature* 407(6802):340–348.

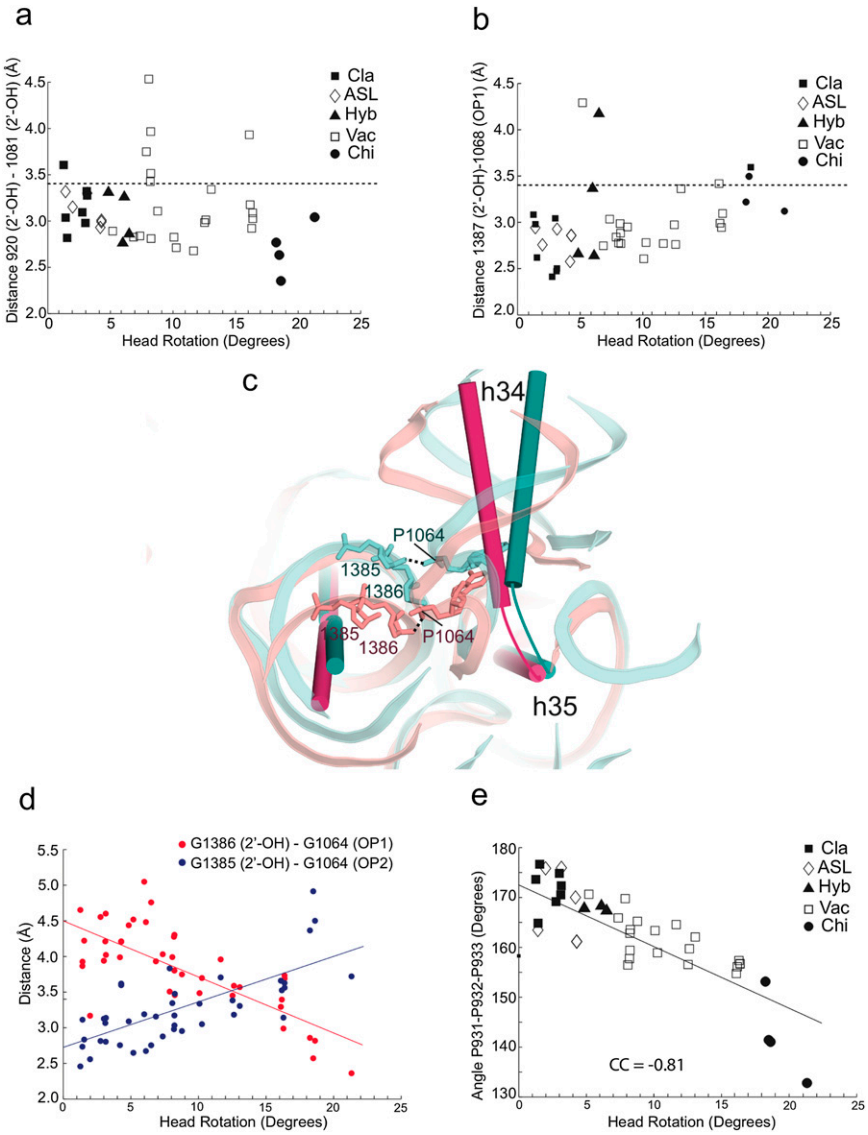

Fig. S6. Contacts between hinges. The two parallel helical systems containing hinges 1 and 2 remain in contact with each other (d < 3.4 Å) through various degrees of 30S head rotation for most structures. (*A*) Ribose 920 (2′-OH) at the junction of h28 and h2 contacts ribose 1081 (2′-OH) in h36, and (*B*) ribose 1387 (2′-OH) in h28 contacts P1068 (OP1) at the apex of h35. (*C*) Change in the position of h34 with head rotation (Chi is in magenta and Cla in teal); helix h34 swivels toward h28, disrupting contacts between h34 and h28. (*D*) P1064 (OP2) in h34 switches its H-bonded contact with h28 from ribose 1385 (2′-OH) to ribose 1386 (2′-OH), correlated with an increase in head rotation. (*E*) The angle subtended by P931–P932–P933 decreases as the head rotates, suggesting that the switch in contact between h28 and h34 is coupled to this backbone deformation.

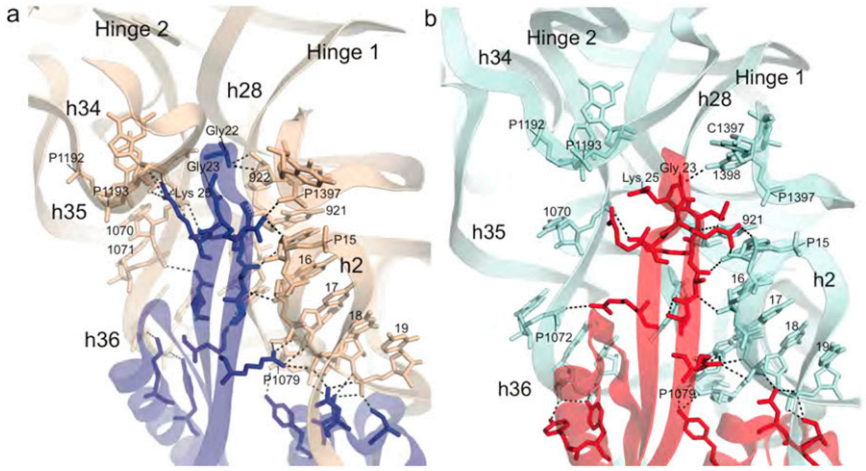

Fig. S7. Protein S5 contacts static elements of both hinges. (*A*) In the classical state (1), protein S5 (blue) interacts extensively with both sets of 16S rRNA (gold) head–body connectors, at their points of connection; that is, S5 interacts with h36 where it docks into h2, as well as with helices h2 and h35 and the static portion of h28, which is approximately coaxial with h2 (Fig. 2). Additionally, in the classical state, the tip of the β-hairpin loop of S5 contacts 16S rRNA h34 at positions 1192 and 1193 via Lys-25. (*B*) In the chimeric hybrid state (2), S5 (red) largely maintains its contacts with helices h2 and h35/h36 in the 16S rRNA (cyan). However, all contacts between S5 and h34 are disrupted due to the swiveling movement of h34 during head rotation.

1. Jenner LB, Demeshkina N, Yusupova G, Yusupov M (2010) Structural aspects of messenger RNA reading frame maintenance by the ribosome. *Nat Struct Mol Biol* 17(5):555–560.
2. Zhou J, Lancaster L, Donohue JP, Noller HF (2013) Crystal structures of EF-G-ribosome complexes trapped in intermediate states of translocation. *Science* 340(6140):1236086.

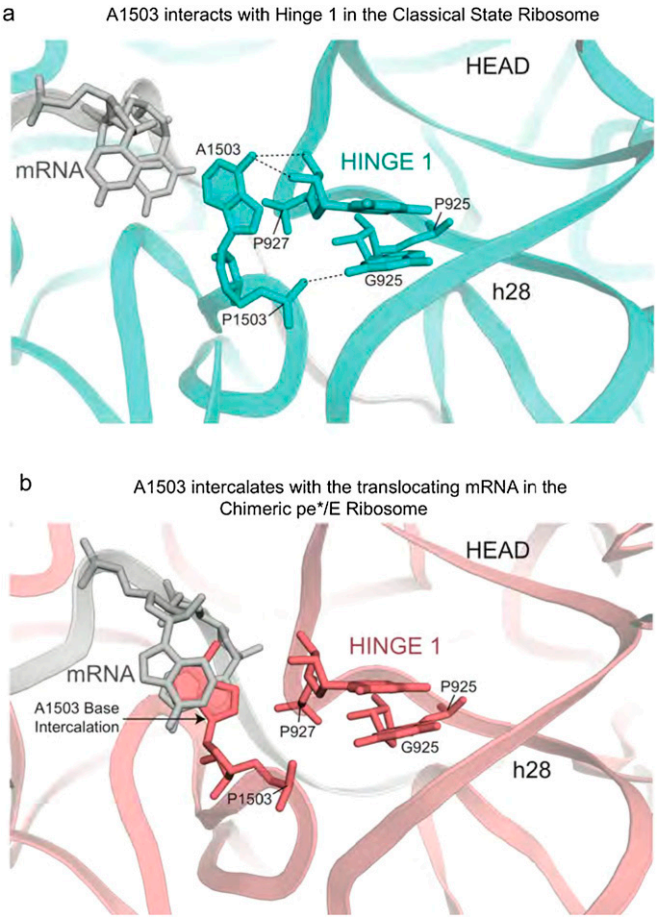

Fig. S8. Hinge 1 and the mRNA translocation control. It has been recently suggested that A1503 may act as a transcriptional pawl by intercalating with the mRNA (1) in chimeric hybrid ribosome complexes with large head rotations. (*A*) In most structures, A1503 interacts with hinge 1 at positions G925 and G927, as shown here for a classical-state complex (2) (PDB ID code 3I8H). 16S rRNA is in blue and mRNA in gray. (*B*) In the chimeric hybrid structures (such as, PDB ID code 4KBT) (1), A1503 no longer contacts hinge 1; instead it intercalates with the mRNA between positions -1 and -2 (gray).

1. Zhou J, Lancaster L, Donohue JP, Noller HF (2013) Crystal structures of EF-G-ribosome complexes trapped in intermediate states of translocation. *Science* 340(6140):1236086.
2. Yusupova G, Jenner L, Rees B, Moras D, Yusupov M (2006) Structural basis for messenger RNA movement on the ribosome. *Nature* 444(7117):391–394.

Table S1. 30S head and body rotations in ribosome complexes

Refs.	PDB ID code	Head rotation	Body rotation	tRNA	Factors	Antibiotics	Organism	Group[†]	Resolution, Å
Selmer et al. (2006) (1)	2J00[‡]	0	0	A, P, E	—	Par	Tth	Cla	2.8
Jenner et al. (2010) (2)	3I8H	1.3	1	A, P, E	—	—	Tth	Cla	3.1
Zhang et al. (2009) (3)	3I1Z	1.4	5.2	A-ASL, P-ASL	—	—	Eco	—	3.7
Stanley et al. (2010) (4)	3KNJ	1.4	−0.5	A, P, E	—	Vio, Cap	Tth	Cla	3.2
Dunkle et al. (2011) (5)	4GD2	1.5	−1.2	P	—	—	Eco	Cla	3
Rabl et al. (2011) (6)	2XZN[§,¶]	1.7	—	—	eIF-1	—	Tet	—	3.9
Zhang et al. (2009) (3)	3I1Q	2	4.9	P-ASL	—	—	Eco	—	3.8
Berk et al. (2006) (7)	2I2U	2	4.3	P-ASL	—	—	Eco	—	3.2
Feng et al. (2013) (8)	4B8F	2.8	−1	P, E	EF-G·GDP	—	Tth	Cla	3.7
Laurberg et al. (2008) (9)	3D5A	3	−1.7	P, E	RF-1	—	Tth	Cla	3.2
Yusupov et al. (2001) (10)	1GIX	3.1	−2.3	A, P, E	—	—	Tth	—	5.5
Gao et al. (2009) (11)	2WRI	3.1	−1.2	P, E	EF-G·GDP	Fus	Tth	Cla	3.6
Korostelev et al. (2008) (12)	3F1G	3.1	−1.2	P, E	RF-2	—	Tth	Cla	3
Zhang et al. (2009) (3)	3I21	3.2	−1.5	A-ASL, P-ASL	—	—	Eco	—	3.7
Agirrezabala et al. (2012) (13)	3J0U	3.3	1.7	A, P (class 2)	—	—	Eco	—	12.1[‖]
Agirrezabala et al. (2012) (13)	3J13	4	0.6	P (class 3)	—	—	Eco	—	13.1[‖]
Berk et al. (2006) (7)	2I2P	4.3	−2.7	P-ASL	—	—	Eco	—	3.2
Brilot et al. (2013) (14)	3J5X	4.8	9.7	A/P*, P/E	EF-G·GDP	Vio	Eco	—	7.6[‖]
Dunkle et al. (2011) (5)	4GD1	4.8	8.4	P/E	RRF	—	Eco	Hyb	3
Jin et al. (2011) (15)	3ZVO	6	8.8	P/E	RF3·GTP	—	Tth	Hyb	3.8
Agirrezabala et al. (2012) (13)	3J0V	5.9	2.9	A, P (class 4a)	—	—	Eco	—	14.7[‖]
Ratje et al. (2010) (16)	2XSY	6.1	6	P/E	EF-G·GDP	Fus	Tth	—	7.8[‖]
Chen et al. (2013) (17)	4CR1	6.1	7	P/E	EF-G·GDPCP	Fus	Tth	Hyb	3.0
Tourigny et al. (2013) (18)	4JUW	6.5	6.3	P/E	EF-G·GDPCP	—	Tth	Hyb	2.9
Pulk et al. (2013) (19)	4KIY	6.9	3.1	—	EF-G·GDPCP	Vio	Eco	—	2.9
Agirrezabala et al. (2012) (13)	3J0Z	6.9	8.5	A/A, P/E (class 5)	—	—	Eco	—	11.5[‖]
Agirrezabala et al. (2012) (13)	3J10	7	7.7	A/A, P/E (class 6)	—	—	Eco	—	11.5[‖]
Agirrezabala et al. (2012) (13)	3J0X	7.2	5.1	A/A, P/E (class 4b)	—	—	Eco	—	13.5[‖]
Pulk et al. (2013) (19)	4KJ2	7.4	2.1	—	EF-G·GDPCP	Vio	Eco	—	2.9
Pulk et al. (2013) (19)	4KJ0	7.6	2.3	—	EF-G·GDPCP	Vio	Eco	—	2.9
Borovinskaya et al. (2007) (20)	2QOU	7.9	−3.3	—	—	Spc	Eco	Vac1	3.9
Borovinskaya et al. (2008) (21)	3DF1	8	−3.3	—	—	Hyg B	Eco	Vac1	3.5
Schuwirth et al. (2006) (22)	1VS5	8.2	−3.3	—	—	Ksg	Eco	Vac1	3.5
Schuwirth et al. (2005) (23)	2AVY	8.2	−3.3	—	—	—	Eco	Vac1	3.5
Borovinskaya et al. (2007) (20)	2QBD	8.2	−3.5	—	—	—	Eco	Vac1	3.3
Zhang et al. (2009) (3)	3I1O	8.8	−1.3	—	—	—	Eco	—	3.2
Pulk et al. (2013) (19)	4KJ8	10.1	2.4	—	EF-G·GDPCP	Vio	Eco	Vac2	2.9
Pulk et al. (2013) (19)	4KJ6	10.3	3.8	—	EF-G·GDPCP	Vio	Eco	Vac2	2.9
Zhang et al. (2009) (3)	3I1M	11.6	5	—	—	—	Eco	—	3.2
Pulk et al. (2013) (19)	4KJC	12.5	7.2	—	EF-G·GDPCP	Vio	Eco	Vac2	2.9
Pulk et al. (2013) (19)	4KJA	12.6	−2.6	—	EF-G·GDPCP	Vio	Eco	—	2.9
Pulk et al. (2013) (19)	4KJ4	13.1	6.2	—	EF-G·GDPCP	Vio	Eco	Vac2	2.9
Ben-Shem et al. (2011) (24)	3U5B[§]	16	—	—	—	—	Sce	Vac3	3
Borovinskaya et al. (2008) (21)	3DF3	16.1	−2.3	—	—	Hyg B	Eco	Vac3	3.5
Borovinskaya et al. (2007) (20)	2QBF	16.2	−2.5	—	RRF	—	Eco	Vac3	3.3
Rabl et al. (2011) (6)	2XZM[§]	16.2	—	—	eIF-1	—	Tet	—	3.9
Zhou et al. (2012) (25)	3SFS	16.3	6.8	—	RF3·GDPNP	Vio	Eco	—	3.2
Schuwirth et al. (2006) (22)	1VS7	16.4	−2.3	—	—	Ksg	Eco	Vac3	3.5
Schuwirth et al. (2005) (23)	2AW7	16.4	−2.3	—	—	—	Eco	Vac3	3.5
Zhou et al. (2013) (26)	4KCY	18.2	1.3	pe/E	EF-G·GDPNP	Vio	Tth	Chi	3.5
Ramrath et al. (2013) (27)	3J5N	18.4	2.5	ap/P, pe/E	EF-G·GDP	Fus	Eco	—	6.8[‖]
Zhou et al. (2013) (26)	4KD8	18.5	1.3	pe/E	EF-G·GDP	Fus, Vio	Tth	Chi	3.5
Zhou et al. (2013) (26)	4KDG	18.6	1.1	pe/E	EF-G·GDP	Fus	Tth	Chi	4
Ratje et al. (2010) (16)	2XUY	20.7	3	pe/E	EF-G--GDP	Fus	Tth	—	7.6[‖]
Zhou et al. (2013) (26)	4KBT	21.3	3.4	pe/E	EF-G·GDPNP	Vio	Tth	Chi	3.9

Identification of head rotation hinges was done using the above six groups (Fig. 2). However, all 41 bacterial structures (i.e., excluding eukaryotic structures and the low-resolution structures 1GIX, 2XSY, 2XUY, 3J5X, 3J5N, 3J5T, 3J0U, 3J13, 3J0Z, 3J10, and 3J0X) were used in nucleotide-level analyses. See *SI Methods* for details. A, aminoacyl site; Cap, capreomycin; Chi, chimeric pe/E or ap/P state; Cla, classical state; E, exit site; Eco, *E. coli*; Fus, fusidic acid; Hyb, P/E or A/P hybrid state; Hyg B, hygromycin B; Ksg, kasugamycin; P, peptidyl site; Par, paromomycin; Tet, *Tetrahymena thermophila*; Tth, *Thermus thermophilus*; Vac1–3, vacant ribosomes 1–3; Vio, viomycin.

[†]Bacterial crystal structures were grouped by similar head and body rotations and similar conformational state of the bound tRNA.

[‡]PDB ID code 2J00 was used as the reference structure, defined as 0° head and body rotation.

[§]Eukaryotic structures.

[¶]Reference structure for eukaryotic head rotation calculations.

[‖]Cryo-EM–derived ribosome structures.

1. Selmer M, et al. (2006) Structure of the 70S ribosome complexed with mRNA and tRNA. *Science* 313(5795):1935–1942.
2. Jenner LB, Demeshkina N, Yusupova G, Yusupov M (2010) Structural aspects of messenger RNA reading frame maintenance by the ribosome. *Nat Struct Mol Biol* 17(5):555–560.
3. Zhang W, Dunkle JA, Cate JHD (2009) Structures of the ribosome in intermediate states of ratcheting. *Science* 325(5943):1014–1017.
4. Stanley RE, Blaha G, Grodzicki RL, Strickler MD, Steitz TA (2010) The structures of the anti-tuberculosis antibiotics viomycin and capreomycin bound to the 70S ribosome. *Nat Struct Mol Biol* 17(3):289–293.
5. Dunkle JA, et al. (2011) Structures of the bacterial ribosome in classical and hybrid states of tRNA binding. *Science* 332(6032):981–984.
6. Rabl J, Leibundgut M, Ataide SF, Haag A, Ban N (2011) Crystal structure of the eukaryotic 40S ribosomal subunit in complex with initiation factor 1. *Science* 331(6018):730–736.
7. Berk V, Cate JHD (2007) Insights into protein biosynthesis from structures of bacterial ribosomes. *Curr Opin Struct Biol* 17(3):302–309.
8. Feng S, Chen Y, Gao YG (2013) Crystal structure of 70S ribosome with both cognate tRNAs in the E and P sites representing an authentic elongation complex. *PLoS ONE* 8(3):e58829.
9. Laurberg M, et al. (2008) Structural basis for translation termination on the 70S ribosome. *Nature* 454(7206):852–857.
10. Yusupov MM, et al. (2001) Crystal structure of the ribosome at 5.5 A resolution. *Science* 292(5518):883–896.
11. Gao Y-G, et al. (2009) The structure of the ribosome with elongation factor G trapped in the posttranslocational state. *Science* 326(5953):694–699.
12. Korostelev A, et al. (2008) Crystal structure of a translation termination complex formed with release factor RF2. *Proc Natl Acad Sci USA* 105(50):19684–19689.
13. Agirrezabala X, et al. (2012) Structural characterization of mRNA-tRNA translocation intermediates. *Proc Natl Acad Sci USA* 109(16):6094–6099.
14. Brilot AF, Korostelev AA, Ermolenko DN, Grigorieff N (2013) Structure of the ribosome with elongation factor G trapped in the pretranslocation state. *Proc Natl Acad Sci USA* 110(52): 20994–20999.
15. Jin H, Kelley AC, Ramakrishnan V (2011) Crystal structure of the hybrid state of ribosome in complex with the guanosine triphosphatase release factor 3. *Proc Natl Acad Sci USA* 108(38):15798–15803.
16. Ratje AH, et al. (2010) Head swivel on the ribosome facilitates translocation by means of intra-subunit tRNA hybrid sites. *Nature* 468(7324):713–716.
17. Chen Y, Feng S, Kumar V, Ero R, Gao Y-G (2013) Structure of EF-G-ribosome complex in a pretranslocation state. *Nat Struct Mol Biol* 20(9):1077–1084.
18. Tourigny DS, Fernández IS, Kelley AC, Ramakrishnan V (2013) Elongation factor G bound to the ribosome in an intermediate state of translocation. *Science* 340(6140):1235490.
19. Pulk A, Cate JHD (2013) Control of ribosomal subunit rotation by elongation factor G. *Science* 340(6140):1235970.
20. Borovinskaya MA, Shoji S, Holton JM, Fredrick K, Cate JHD (2007) A steric block in translation caused by the antibiotic spectinomycin. *ACS Chem Biol* 2(8):545–552.
21. Borovinskaya MA, Shoji S, Fredrick K, Cate JH (2008) Structural basis for hygromycin B inhibition of protein biosynthesis. *RNA* 14(8):1590–1599.
22. Schuwirth BS, et al. (2006) Structural analysis of kasugamycin inhibition of translation. *Nat Struct Mol Biol* 13(10):879–886.
23. Schuwirth BS, et al. (2005) Structures of the bacterial ribosome at 3.5 A resolution. *Science* 310(5749):827–834.
24. Ben-Shem A, et al. (2011) The structure of the eukaryotic ribosome at 3.0 Å resolution. *Science* 334(6062):1524–1529.
25. Zhou J, Lancaster L, Trakhanov S, Noller HF (2012) Crystal structure of release factor RF3 trapped in the GTP state on a rotated conformation of the ribosome. *RNA* 18(2):230–240.
26. Zhou J, Lancaster L, Donohue JP, Noller HF (2013) Crystal structures of EF-G-ribosome complexes trapped in intermediate states of translocation. *Science* 340(6140):1236086.
27. Ramrath DJF, et al. (2013) Visualization of two transfer RNAs trapped in transit during elongation factor G-mediated translocation. *Proc Natl Acad Sci USA* 110(52):20964–20969.